



The effect of sunlight induced surface defects on the photocatalytic activity of nanosized CeO₂ for the degradation of phenol and its derivatives

M. Aslam^a, M.T. Qamar^{a,b}, M.Tahir Soomro^a, Iqbal M.I. Ismail^{a,b}, Numan Salah^c, Talal Almeelbi^{a,d}, M.A. Gondal^e, A. Hameed^{a,f,*}

^a Centre of Excellence in Environmental Studies (CEES), King Abdulaziz University, Jeddah 21589, Saudi Arabia

^b Chemistry Department, Faculty of Science, King Abdulaziz University, P.O. Box 80203, Jeddah 21589, Saudi Arabia

^c Centre of Nanotechnology, King Abdulaziz University, Jeddah 21589, Saudi Arabia

^d Department of Environmental Sciences, King Abdulaziz University, Jeddah 21589, Saudi Arabia

^e Department of Physics, King Fahd University of Petroleum and Minerals, Dhahran 31261, Saudi Arabia

^f National Centre for Physics, Quaid-e-Azam University, Islamabad 44000, Pakistan

ARTICLE INFO

Article history:

Received 26 March 2015

Received in revised form 1 June 2015

Accepted 26 June 2015

Available online 2 July 2015

Keywords:

Sunlight photocatalysis

Nanosized CeO₂

Surface defects

Phenol

2-CP

2-NP

2-BP

ABSTRACT

The photocatalytic activity of nanostructured CeO₂ was investigated for the degradation of phenol and its derivatives (2-chlorophenol, 2-bromophenol and 2-nitrophenol) in the exposure of complete spectrum and visible region (420–800 nm) of sunlight. The adopted experimental parameters imparted high crystallinity, phase purity, controlled morphology and uniform particle size of ~11 nm to the synthesized CeO₂. During the evaluation of the photocatalytic activity, the initial low degradation of the substrates till the 90 min of complete spectrum sunlight exposure followed by a piercing increase predicted the favorable photon induced surface changes in CeO₂. The careful examination of the exposed and unexposed CeO₂ by spectroscopic techniques (diffuse reflectance (DR), photoluminescence (PL), ATR-FTIR and Raman spectroscopy) and electrochemical tools (cyclic voltammetry (CV), electrochemical impedance spectroscopy (EIS) and chronopotentiometry (CP)) revealed the vital role of photon induced surface phases for the improved spectral response and suppressed charge carriers recombination process. Based on the appearance of additional weak reflection at $2\theta = 28.15^\circ$ in the X-ray diffraction (XRD) pattern and inhalation of O₂ in the thermogravimetric analysis (TGA) of sunlight exposed samples revealed the prevalence of photon induced defects generated by the departure of surface oxygen from CeO₂. The induction of defects composed of CeO_{2-x} states resulted in the improved activity of the exposed compared to unexposed CeO₂ in the visible spectrum (420–800 nm) of sunlight. The efficient degradation of 2-CP, 2-BP and 2-NP compared to a mild degradation for phenol, in the complete spectrum sunlight exposure, indicated the facilitating role of substituents attached to the aromatic system in the degradation process. The monitoring of the photocatalytic degradation process by HPLC and identification of intermediates by GC–MS analysis revealed the formation of aromatic intermediates in the degradation of phenol and 2-BP while no aromatic intermediate was identified in the degradation of 2-NP and 2-CP. The rapid disappearance of the total carbon and further oxidation of released anions supported the major role of superoxide anion radicals in the oxidation process. Both pure and sunlight exposed CeO₂ exhibited sustained photocatalytic activity in the repeated exposures.

© 2015 Elsevier B.V. All rights reserved.

1. Introduction

The potential of photon initiated oxidation processes especially that of photocatalysis, for the elimination of organic contaminants is well established [1–5]. The conspicuous features of this technology is the use of nontoxic photocatalysts, inexpensive photons, soft operation conditions and complete mineralization. Being strictly

* Corresponding author at: Centre of Excellence in Environmental Studies (CEES), King Abdulaziz University, Jeddah 21589, Saudi Arabia. Fax: +966 1 2 6952674.

E-mail addresses: afmuhammad@kau.edu.sa, hameedch@yahoo.com (A. Hameed).

dependent on the uninterrupted supply of photons, being cost effective and ever renewable, the use of sunlight for actuating photocatalysts is a rational approach. In the area of photocatalysis research, TiO_2 and ZnO , being non-toxic, chemically inert and stable under varying experimental conditions, are the most widely explored photocatalysts for various applications [6–10]. However, TiO_2 suffers disadvantages of low efficiency for sunlight utilization due to the wide band gap, low quantum efficiency and high recombination rate of charge carriers, whereas ZnO , although supports better absorption of photons compared to TiO_2 but experiences anodic dissolution under illumination [11]. Keeping in view the excellent photocatalytic ability of these two catalysts in the UV region, the scientific community has exerted their efforts in extending their absorption cross-section and productivity in the visible region for maximum harvesting of photons. Consequently, the other pure photocatalysts like Bi_2O_3 , WO_3 , V_2O_5 , MnO and CeO_2 has been ignored. In some available studies, Bi_2O_3 , WO_3 and V_2O_5 [12–15] has established their candidacy as suitable sunlight active photocatalysts therefore, in this study, we evaluated the photocatalytic activity of pure CeO_2 in sunlight exposure for the degradation of stable phenolic substrates.

Cerium oxide (CeO_2) is widely used in conventional catalysis for a variety of applications, but least studied for its photocatalytic properties. Being stable and non-toxic, CeO_2 , an n -type semiconductor in nature, has several features that designate it as a potential contender for photocatalytic applications [16]. The electrical, optical and chemical properties of CeO_2 closely resembles to that of TiO_2 . CeO_2 has a band gap ranged between 2.9 and 3.2 eV (depending on the morphology and particle size) but compared to TiO_2 , possesses a sufficiently long lifetime of photogenerated electron–hole pairs [17]. The photocatalytic activity of CeO_2 under visible exposure has been shown recently in the presence of industrially relevant dyes such as naphthol blue and acidic black [18,19]. Few studies are available in the literature regarding the photocatalytic activity of pure CeO_2 in sunlight, especially phenols [20,21].

The toxicity and carcinogenicity of phenol derivatives demands their prompt removal from the water for living being consumption [22]. A wide variety of treatment methods for the removal of phenolic compounds from the contaminated water are in use, however, every treatment option suffer from major drawbacks of strict maintenance of operating conditions and possibility of formation of more toxic intermediates [23–29]. Among phenol derivatives, chloro, bromo and nitrophenols are the most important water contaminants [30–34]. Nitrophenols, due to the high stability and solubility imparted by NO_2 group, are resistant to degradation and transform into more toxic off shoots [6,35,36]. The toxicity and jeopardies of chlorophenols are well recognized which depends on the position of the chloro group with respect to the phenolic hydroxyl group [37,38]. The major portion of the studies available on the degradation of phenol and its derivatives are carried out in the presence of TiO_2 . No comprehensive study covering all the aspects on the photocatalytic removal of phenol and its derivatives over CeO_2 in sunlight is available.

In the present study, we developed a user friendly procedure for the synthesis of pure nanosized CeO_2 using Triton® X-100 (as surfactant) and evaluated its efficacy for the removal of phenol and its derivatives (2-chlorophenol, 2-bromophenol and 2-nitrophenol). The choice of the phenol derivatives was based on the nature of the substituent attached to 2- position of the carboxylic acid. The drop-off in the concentration of phenolic substrates and variations in intermediates was monitored by HPLC while the intermediates were identified by GC–MS. The removal of total organic carbon and release of respective anions and their further oxidation was also monitored. The observed changes in CeO_2 in the sunlight exposure and their effect on the photocatalytic activity were investigated by optical, structural and morphological investigative tools and

the possible reasons for the formation of photon induced defects and their role in enhancing the photocatalytic activity were also discussed.

2. Experimental details

CeO_2 nanoparticles were synthesized by dissolving $\text{Ce}(\text{NO}_3)_3 \cdot 6\text{H}_2\text{O}$ (Sigma–Aldrich) (99.99% pure) in deionized water under stirring. Triton® X-100 (0.05%) with respect to the weight of the Ce^{3+} ions was added to the metal ion solution and stirred for three hours at 80°C for complete micelle formation. The metal ion solution was slowly hydrolyzed with 0.25 M KOH solution and adjusted the pH at 8. The precipitates/gel was heated at 250°C till the utter transformation of gel to precipitates. The precipitates were filtered, rinsed with Milli-Q water and acetone/ethanol mixture (50:50) for complete removal of surfactant and dried in hot air oven overnight. The dried powder was ground and calcined at 500°C in a muffle furnace for 6 h that resulted in pale yellow CeO_2 powder.

A PerkinElmer UV–vis diffuse reflectance spectrophotometer (DRS) recorded the solid-state absorption and diffuse reflectance spectra of CeO_2 nanoparticles before and after the sunlight exposure in 200–900 nm wavelength range. The bandgaps were evaluated by applying Kubelka–Munk transformation, $F(R)$, on %R data initially and by plotting $(F(R) \times h\nu)^{1/2}$ versus $h\nu$ finally. The photoluminescence (PL) spectra of the unexposed and exposed CeO_2 were recorded by a fluorescence spectro-fluorophotometer, RF-5301 PC, Shimadzu, Japan at an excitation wavelength of 325 nm and slit width of 10 nm. ATR-FTIR analysis were performed with FTIR spectrometer, IRAffinity-1, Shimadzu, Japan equipped with ATR-8200H from PIKE technologies. Raman shifts were measured using a DXR Raman Microscope, Thermo Scientific, USA, equipped with 532 nm laser as the excitation source at 6 mW power.

A VSP multi-channel potentiostat (Bio-logic Science Instrument, USA) was employed for electrochemical measurements in the dark and under illumination. An electrochemical cell with three-electrode system (a glassy carbon electrode (GCE), a saturated calomel reference electrode (SCE), and a Pt wire counter electrode) was used. For illumination a 50 W halogen lamp was used. All the solution were prepared using 0.1 M KCl electrolyte. Electrochemical impedance spectroscopy (EIS) was performed at open circuit voltage (OCV) by scanning the frequency from 0.1 Hz to 10 kHz. The EIS Nyquist plots were fitted by Zfit (Ec-lab software, Bio-logic Science Instruments, USA). The drop coating method was used for the modification of GCE [39,40]. The homogenized suspension of 1 mg of the photocatalyst in 1 ml of deionized water was casted at the tip of the GCE by dropping 20 μL , dried to film by hot air drying. The uniformity of the film was examined optically.

The thermo-gravimetric profiles of pure and sunlight exposed CeO_2 were recorded in air flow (40 ml/min) by SHIMADZU thermal analyzer in the range of 50 – 950°C at a heating rate of 10°C per min. Xpert X-ray powder diffractometer (Philips PW1398) with Cu K α radiation source was used to record the XRD patterns from 20° to 80° (2θ) with a step size of 0.05° . The crystallite size were measured by applying Scherer's equation on main reflections. The morphology and particle size of the synthesized powder was examined by Field emission scanning electron microscope (FESEM) (JEOL JSM 6490-A) at different resolutions.

The photocatalytic activity of CeO_2 nanoparticles for the degradation of phenolic substrates in complete spectrum and visible region (420–800 nm) of sunlight was investigated by exposing the CeO_2 –phenol suspension containing 150 ml (50 ppm) of respective phenol solution and the optimized amount of 200 mg of CeO_2 . The amount of the catalyst and the concentration of phenolic substrate solutions were kept constant for comparison. All the experiments

were performed in the sunlight illumination of $900 \pm 100 \times 10^2$ lx and fixed period of the daylight. All the experiments were studied for a period of 180 min. A 10 ml sample was taken out after every 30 min in the first 2 h and after 60 min in the third hour. The experiments in the visible region of the sunlight were performed by adopting the above-mentioned procedure using a Pyrex glass reactor. The dimensions of the glass reactor were 15.5 (diameter) \times 2.5 (height) and the evaluated effective surface area of the reactor was 189 cm². The samples, after removing the catalyst, were analyzed by HPLC (SPD-20A, Shimadzu Corporation, Japan), TOC (Shimadzu Corporation, Japan) and IC (Thermo Scientific, USA). For GC–MS analysis the samples collected after 30 min of exposure were extracted thrice with 10 ml of dichloromethane (Sigma–Aldrich, 99.99%) and dried with anhydrous magnesium sulfate for complete removal of water. A GC–MS (Shimadzu Corporation, Japan, Shimadzu-QP2010 Plus) equipped with RtX1 capillary column, for the identification of unknown compounds formed as intermediate during the degradation process.

3. Results and discussion

3.1. Photocatalytic degradation of phenolic substrates

The illumination of semiconductor powder in the aqueous system leads to the generation of a variety of radical and charged species. The hydroxyl radicals (OH•) and the charged superoxide anion radicals (O₂•[−]) are regarded as the major contributors in the reactive oxygen species (ROS) generated in the photocatalytic system [4,41]. Hydroxyl radicals are originated because of water oxidation by the photogenerated holes (h⁺), whereas superoxide anions are instigated from oxygen reduction by photo-excited (e[−]) conduction band electrons. The suitability of the electrochemical potentials of valence and conduction band edges is one of the key controlling factors in the production of these two entities. The generation of OH• and O₂•[−] radicals can be represented by the equations given below.



The oxidizing power of these species is very well established and until recently, hydroxyl radicals were recognized as the major oxidants in the photocatalytic system however, some recent reports proposed the leading role of superoxide anion radicals (O₂•[−]) [41]. In the current study, besides evaluating the power of CeO₂ for the degradation of a variety of phenolic substrates in complete spectrum and visible region of the sunlight, based on the experimental results, we attempted to ascertain the major contributor either hydroxyl or superoxide anion radicals, in the degradation process.

The percentage degradation of phenol, 2-CP, 2-BP, and 2-NP as a function of complete spectrum sunlight exposure time is presented in Fig. 1a, where, in comparison to pure phenol, a significantly higher degradation of 2-CP, 2-BP and 2-NP was noticed. In the initial 30 min of sunlight exposure, compared to ~5% decrease in the concentration of phenol, a ~35%, ~27% and ~37% degradation of 2-CP, 2-BP and 2-NP was observed, respectively. After 180 min of sunlight exposure ~98%, ~96% and ~99% of 2-CP, 2-BP and 2-NP were removed, respectively, whereas <35% degradation was noticed for phenol in the same period.

The HPLC profiles of phenol, 2-CP, 2-BP and 2-NP in the exposure of complete spectrum of sunlight are presented in Fig. S1 (Supporting information), where the appearance of intermediates revealed that the substrates are not mineralized directly rather initially degraded with the formation of intermediates. It is also evident from the comparison of the HPLC degradation profiles of phenol and 2-BP that phenol is formed as intermediate in the degra-

dation of 2-BP, whereas the degradation of 2-CP and 2-NP proceeds without the formation of aromatic intermediates.

Fig. 1c shows the rate profiles of the phenolic substrates obtained by plotting $\ln(C_0/C)$ versus the sunlight exposure time “t”. Except for pure phenol, a complete deviation from the Langmuir–Hinshelwood kinetic model for pseudo first order reactions was witnessed for 2-CP, 2-BP and 2-NP, where a low rate of degradation followed by an increase afterwards was noticed. Based on the above-mentioned finding, it was presumed that the absorption of photons induces prolific changes in CeO₂ that led to the enhanced generation of reactive oxygen species (ROS) and accelerated degradation of phenolic substrates. Interestingly, the above mentioned observations were not perceived in the experiments performed in the visible region (420–800 nm) of sunlight by obstructing the UV photons rather a significant decrease in the removal of all the phenolic substrates (phenol, 2-CP, 2-BP and 2-NP) was witnessed. The HPLC degradation profiles of 2-CP, 2-BP and 2-NP in the illumination of the visible region of sunlight are presented in Fig. S2 (Supporting information). In the exposure of visible region of sunlight, an overall decrease of ~35% (Fig. 1b) was noticed in the degradation ability of CeO₂. A minimum degradation of <8% was recorded for phenol. Similar to complete spectrum exposure, the formation of phenol was observed in the degradation of 2-BP in the visible region also. The plot of $\ln(C_0/C)$ versus the exposure time (t) in the visible region of sunlight is shown in Fig. 1d. Noticeably, the rate of degradation of the phenolic substrates followed the Langmuir–Hinshelwood kinetic model and well correlated linear increase was observed in the degradation rate with the increase in the exposure time, which depicted the consistent and steady generation of oxidizing species in the visible region compared to complete spectrum of sunlight.

Fig. 2a shows the percentage TOC removal of the phenolic substrates, in a complete spectrum sunlight exposure. A relatively low TOC removal compared to the degradation exhibited that the phenolic substrates are initially transformed to intermediates that are further subjected to oxidation by ROS leading to complete mineralization. Compared to >35% degradation in the initial 30 min of exposure, ~27%, ~23% and ~30% TOC removal was observed for 2-CP, 2-BP and 2-NP, respectively, which depicted the priority engagement of ROS in the degradation process rather than mineralization. The decreasing residual concentration of phenolic substrates after significant degradation, the TOC removal escalated and in 180 min of sunlight exposure, ~94%, ~91% and ~96% TOC removal was evidenced for 2-CP, 2-BP and 2-NP, respectively. The percentage TOC removal in visible portion exposure (Fig. 2b) was significantly lower than that of complete spectrum sunlight exposure. Compared to ~96% TOC removal for 2-NP in 180 min of complete spectrum sunlight exposure, <70% mineralization was noticed in the same period. As presented in Fig. S3a (Supporting information), a trend similar to that of degradation was observed in the rate of TOC removal evaluated by plotting $\ln(C_0/C)$ versus the sunlight exposure time. A marked increase in the rate of TOC removal was observed with the increase in the sunlight exposure time beyond 90 min. However, this effect was not pronounced in the exposure of the visible region of sunlight spectrum (Fig. S3b, Supporting information). The observation regarding the increase in the rate of degradation and TOC removal in the exposure of complete spectrum as compared to the visible region of sunlight clearly depicted the influence of UV photons in inducing the surface modifications that significantly enhanced the generation of oxidation species involved in the degradation as well as mineralization (TOC removal) process.

To resolve the issue of increased activity of CeO₂ with sunlight exposure time, the CeO₂ nanoparticles were exposed to sunlight in water for 1 h and 3 h and their optical, electrochemical, thermal, structural and morphological properties were compared with that

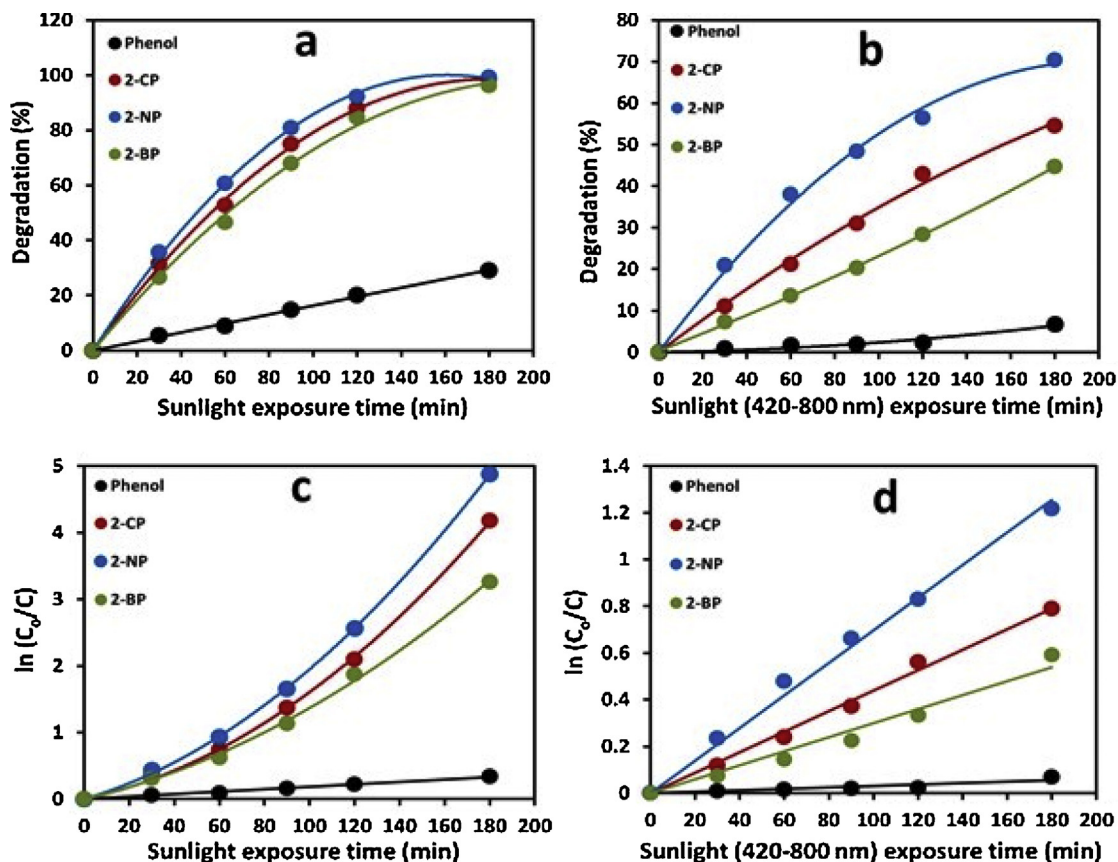


Fig. 1. The comparison of the percentage degradation (a) in sunlight exposure (b) in visible region (420–800 nm) of sunlight of phenol, 2-CP, 2-BP, and 2-NP (50 ppm each). The corresponding plots of $\ln(C_0/C)$ versus exposure time in complete spectrum and visible region (420–800 nm) sunlight exposure are presented in (c) and (d), respectively.

of unexposed CeO_2 . The comparison of the solid-state absorption spectra of unexposed and exposed CeO_2 nanoparticles is shown in Fig. 3a. Compared to unexposed CeO_2 nanoparticles, the sunlight exposed samples exhibited enhanced absorption in the visible region. Additionally, an increase in the extent of absorption in the visible region was noticed with the increase in exposure time that depicted the increased formation of visible photons absorptive entities. The graphical evaluation of the bandgap of unexposed and exposed CeO_2 (inset of Fig. 3a) revealed the red shift in the bandgap of sunlight exposed compared to unexposed CeO_2 . The evaluated bandgap of ~ 2.94 eV for pure or unexposed CeO_2 was in good agreement with the literature values [42]. The exposure of the nanoparticles to sunlight in aqueous medium for a period of 1 h shifted the bandgap from ~ 2.94 eV to ~ 2.85 eV, while the exposure of 3 h shifted it to ~ 2.6 eV. With the increasing exposure time, the enhanced absorption in the visible region depicted the upsurge in the density of photon induced surface states, whereas the red shift in the bandgap energy verified their supporting role in promoting the low energy excitations. The principal transition in CeO_2 is due to the excitation of electrons from O (2p) to Ce^{4+} (4f) levels, often termed as bandgap excitation. Depending on the stoichiometry of the lattice, the magnitude of this transition ranged between 2.9 and 3.4 eV. For the particular case of sunlight exposed CeO_2 , it may be presumed that the interaction of UV photons of the sunlight resulted in the departure of labile oxygen disturbing the Ce^{4+} – 8O octahedral and formation of Ce^{3+} phases at the surface. The density of Ce^{3+} increases with the increase in sunlight exposure time. The cumulative effect of the transitions i.e. O (2p) to Ce^{4+} (4f) and O(2p) to Ce^{3+} (4f¹) resulted in the shifting of the absorption in the visible region. Additionally, the 4f¹ – 5d⁰ transitions in Ce^{3+} also contribute in this regard.

The major peaks in the PL spectra of the pristine and sunlight exposed CeO_2 appeared at 453 nm, 470 nm, 483 nm, 493 nm and 550 nm (Fig. 3b). The mild variation in the observed values and that reported in the literature [43,44], may be attributed to variation in synthetic route and calcination conditions. Instead of discussing the origin, we concentrated on the variation in the intensity of these emission peaks for pristine and sunlight exposed CeO_2 . The consistent decrease in the intensity of peaks with the exposure time depicted the changes in the surface morphology that imparted extended lifetime to the excited states compared to unexposed CeO_2 .

ATR- FTIR analysis of metal oxides is regarded as a useful tool in identifying the changes in M–O skeleton [45]. A noticeable variation in the intensity of various peaks of unexposed and exposed CeO_2 is observed in Fig. 4a. For unexposed CeO_2 , the major peaks appear at 424.3 cm^{-1} , 445.5 cm^{-1} , 447.1 cm^{-1} , 476.4 cm^{-1} , 495.7 cm^{-1} , 516.9 cm^{-1} , 541.9 cm^{-1} and 584.43 cm^{-1} . Based on the analysis of the intensities of the above mentioned peaks, the peak at 495.7 cm^{-1} was assigned to Ce^{4+} –O stretching vibrations. As the presence of Ce^{3+} states in the pure CeO_2 is equally probable due to the inherited switching between Ce^{4+} and Ce^{3+} states [46,47], the minor peaks at 541.9 cm^{-1} and 584.43 cm^{-1} were assigned to stretching vibration of Ce^{3+} –O bonds. The correlation between the noticeable decrease in the intensity of the peaks 495.7 cm^{-1} and subsequent increase in the intensities of the peaks at 541.9 cm^{-1} and 584.43 cm^{-1} without any noticeable shift in the peak position validated the formation of Ce^{3+} based surface phases with the absorption of UV photons from sunlight.

The peak at ~ 461 cm^{-1} , as observed in the comparison of Raman spectra of unexposed and exposed CeO_2 (Fig. 4b), is the characteristic of the stoichiometric CeO_2 and mainly arises due to the F_{2g}

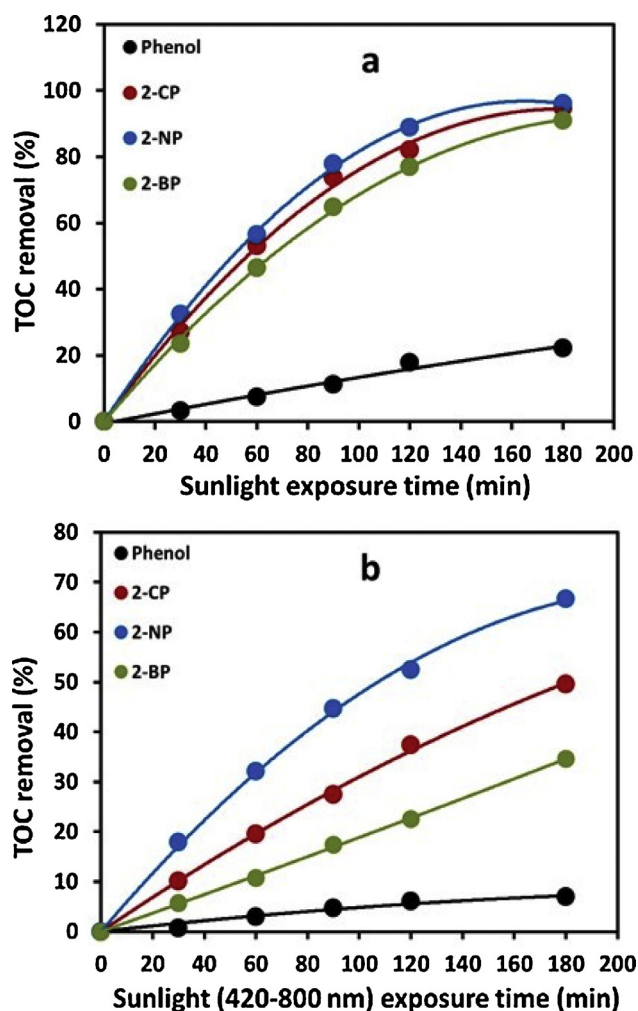


Fig. 2. The comparison of the time scale TOC of phenol, 2-CP, 2-BP, and 2-NP (50 ppm each), in (a) complete spectrum of sunlight and (b) the visible region (420–800 nm) of sunlight.

skeletal vibration of cubic structure [48]. The position of the F_{2g} peak is sensitive to the variations in Ce^{4+} – 8O octahedral arrangement. Compared to unexposed CeO_2 , an increase in the intensity and the shifting of the position toward higher wavelength of F_{2g} peak ($\sim 462.12\text{ cm}^{-1}$ and $\sim 463.09\text{ cm}^{-1}$ for 1 h and 3 h sunlight exposure) for sunlight exposed CeO_2 was evidenced. This observation led to the assumption that the interaction of UV photons of sunlight disturbs the surface cubic structure with the formation of less rigid structures that resulted in the increased intensity and variations in peak position. The exploded view of the comparison of F_{2g} peak positions of unexposed and exposed samples are presented in the inset of Fig. 4b.

The comparison of the XRD patterns of pristine and sunlight exposed (3 h) CeO_2 in the range $2\theta = 20\text{--}80^\circ$ with a step width of 0.05° and scan speed of $4^\circ/\text{min}$ (Fig. 5a), where the sharpness of the peaks was attributed to high crystallinity and phase purity of both the samples. Apart from the decrease in the intensity of the peaks for sunlight exposed CeO_2 , no significant change in the full scale patterns of both the samples was observed. The major reflections for both the samples appeared at 2θ values of 28.51° , 33.02° , 47.36° , 56.28° , 58.97° , 69.40° , 76.73° and 79.22° and matched to “Cerianite (CeO_2)” (PDF# 00-043-1002) with the hkl indices are presented in Fig. 5a. The calculated average crystallite sizes of unexposed and exposed CeO_2 samples were $\sim 11.1\text{ nm}$ and 11.8 nm . As the full scale XRD patterns furnished, no significant information regarding the

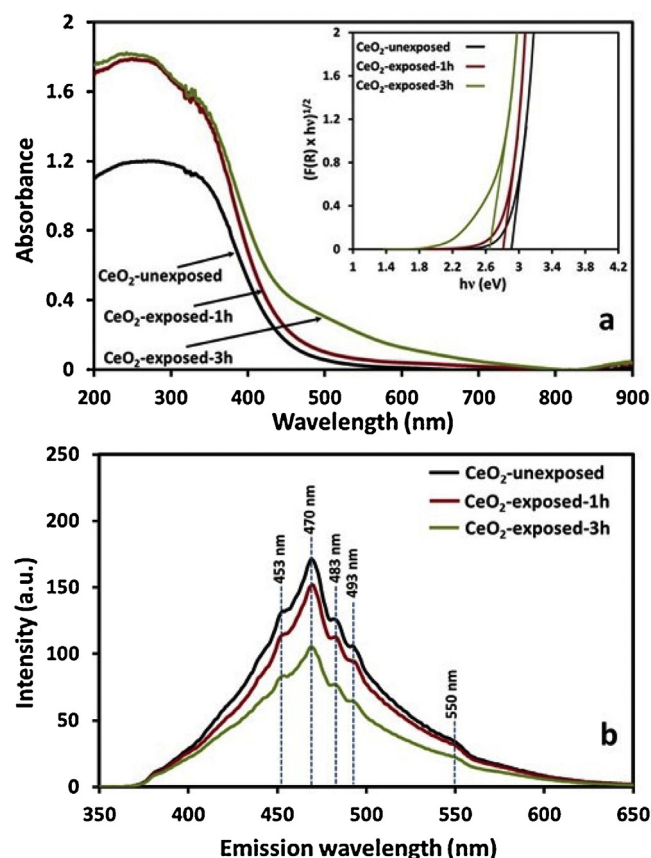


Fig. 3. The comparison of the (a) solid-state absorption spectra (b) PL spectra of unexposed and exposed CeO_2 to sunlight for 1 h and 3 h. The inset of (a) shows the graphical evaluation of the bandgap of unexposed and exposed CeO_2 . The PL spectra were recorded at the excitation wavelength of 325 nm.

formation of photon induced surface phases, the comparison of the individual peaks for both the samples was performed. The comparison of the highly intense peak centered at $2\theta = 28.51^\circ$ in both the patterns, as presented in Fig. 5b and c revealed the appearance of a low intensity shoulder at $2\theta = 28.15^\circ$ that verified the formation of UV photon induced changes at the surface. The same is marked by circle in Fig. 5c for sunlight exposed CeO_2 .

Fig. 6 presents the comparison of the FESEM images of unexposed (a,c,e) and exposed (b,d,f) CeO_2 at $15,000\times$, $30,000\times$ and $60,000\times$, respectively. The observation during the analysis was the excessive surface charging for sunlight exposed compared to unexposed sample. This observation validated the formation of charge excessive Ce^{3+} entities at the surface with $4f^1$ configuration as the source of interaction with the electron beam. The careful analysis of the images at various resolutions revealed the formation of photon induced surface phases without significant disturbance of morphology.

The comparison of the XPS survey scan of the unexposed and exposed CeO_2 is presented in Fig. 7, where all the peaks due to the splitted Ce core levels are observable. The appearance of C1s peak at $\sim 284.9\text{ eV}$ validated the analysis under identical experimental condition. The survey scans were overlapping and it was challenging to estimate the formation of Ce^{3+} surface defects therefore, the high resolution scans of Ce 3d splitted levels in the BE range of $875\text{--}930\text{ eV}$ range were de-convoluted and fitted for the identification of additional peaks and estimation of the variation in the intensity of the existing peaks in the region. The fitted 3d splitted levels of unexposed and exposed CeO_2 powders are presented in Fig. 8a and c. The peaks due to the Ce $3d_{5/2}$ and Ce $3d_{3/2}$ levels

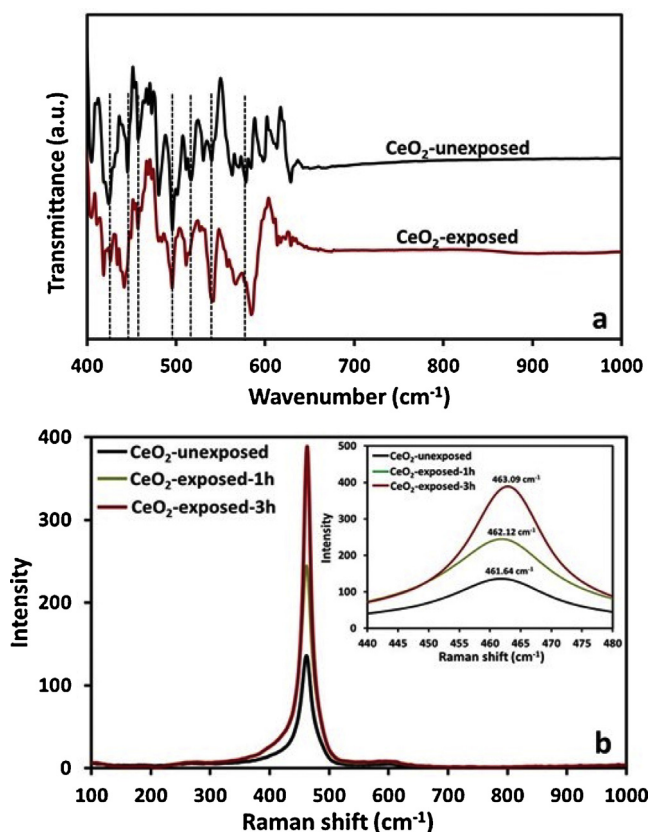


Fig. 4. The comparison of (a) ATR-FTIR spectra and (b) Raman spectra of unexposed and exposed CeO₂ to sunlight for 1 h and 3 h.

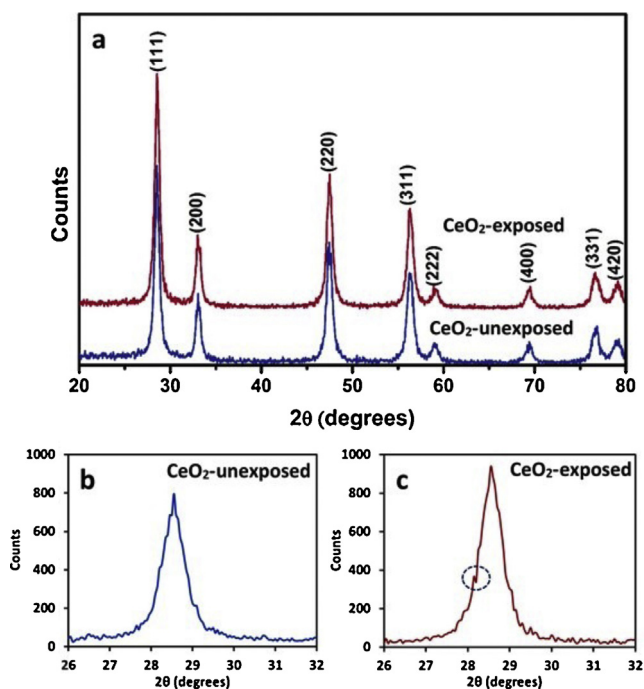


Fig. 5. (a) The comparison of the XRD patterns in the range $2\theta = 20^\circ$ – 80° . The exploded view of the XRD patterns in the range $2\theta = 26^\circ$ – 32° of (b) unexposed and (c) exposed CeO₂. The red circle in (c) indicates the appearance of an additional reflection at $2\theta = 28.15^\circ$. (For interpretation of the references to color in this figure legend, the reader is referred to the web version of this article.)

appear in 875–897 eV and 897–909 eV, respectively, and marked by dotted red lines on the spectrum. The Ce³⁺ and Ce⁴⁺ states coexist in CeO₂ and appear very closely to each other in the XPS pattern. In the current study, the main aim was to verify the formation of the photon induced Ce³⁺ based CeO_{2-x} defects, therefore after identifying the Ce³⁺ states in the spectra of unexposed CeO₂, the results were compared with that of the exposed CeO₂ for the possible variations in the intensity of the existing peaks and appearance of additional peaks. For the unexposed CeO₂, under our experimental conditions, the peaks due to the Ce³⁺ 3d_{5/2} and Ce³⁺ 3d_{3/2} appeared at 892.78 eV and 902.50 eV, respectively, whereas the same for Ce⁴⁺ states appeared at 887.58 eV and 900.71 eV. The observed values in accordance with the literature values [49]. With the minor variation in the position the same peaks were also observed for pre-exposed sample however a significant change in the intensity was noticed. The intensity of the peaks corresponding to Ce⁴⁺ states was reduced, whereas that of Ce³⁺ states was enhanced. With the increase in the Ce³⁺ surface states, a significant augmentation in the intensity of the peak at 902.5 eV, with the minor shift in the position, is observable in the fitted Ce 3d XPS spectra of exposed sample Fig. 8b. The existence of the Ce³⁺ surface states in the form of CeO_{2-x} defects was further verified by the appearance of the shake-up satellite peak at the binding energy of 912.28 eV. The possible effect of the increasing density of CeO_{2-x} defects on the composition of the surface oxygen, the O1s spectra was de-convoluted and presented in Fig. 8c and d. The peaks at 529.28 eV, 530.1 eV and 531.98 eV, in both the samples represented chemically different binding of oxygen with Ce⁴⁺, Ce³⁺ and H, respectively. These findings were in accordance with the previously reported values [50]. A measurable increase in the intensity of the peak at 530.1 eV was noticed for sunlight exposed CeO₂ verifying the increased Ce³⁺ surface states after the exposure as compared to unexposed ceria.

To investigate further, the electrochemical behavior of unexposed and exposed CeO₂, in dark and under illumination, was investigated by cyclic voltammetry (CV), electrochemical impedance spectroscopy (EIS) and chronopotentiometry (CP). Fig. 9a presents the comparison of CV curves obtained by scanning the potential between +1.0 V to –1.0 V for pristine CeO₂ in dark and under illumination. A single reduction peak (Reduction₁) at ~–0.5 V and corresponding oxidation peak (Oxidation₁) at ~0.6 V in the CV pattern was attributed to Ce^{4+/3+} redox pair [51]. The observed minor variations in the cathodic and anodic peak potentials compare to the previously reported values is mainly due to the difference in the experimental parameters [52]. Apart from the enhanced current density response under illumination because of better electron conduction, an additional oxidation peak (Oxidation₂) at ~0.82 V was also observable that may be attributed to the possible changes in the material under illumination. The CV responses of sunlight exposed CeO₂ in the dark and under illumination are presented in Fig. 9b. The cathodic and anodic peaks associated with the Ce^{4+/3+} redox pair become broadened and featureless depicted the possible formation of surface CeO_{2-x}@CeO₂ entities. Additionally, the considerably decreased current density was attributed to the limited electron conduction due the photon induced departure of oxygen. The correlation of the optical characterization by spectroscopic techniques and that of CV analysis revealed a marked improvement in the ability of CeO₂ to suppress the recombination of photogenerated electron–hole pair after being exposed to complete spectrum sunlight for a few hours.

Fig. 10a shows the EIS Nyquist plots of pure as well as sunlight exposed CeO₂ electrodes in the dark and under illumination. The EIS Nyquist plots were analyzed by an equivalent circuit for the electrical response of the pure and exposed CeO₂ electrodes. The obtained EIS parameter (charge transfer resistance) was correlated with the electron–hole pair separation efficiency of the electrodes [53]. As expected from the photocatalytic studies, compared to the dark,

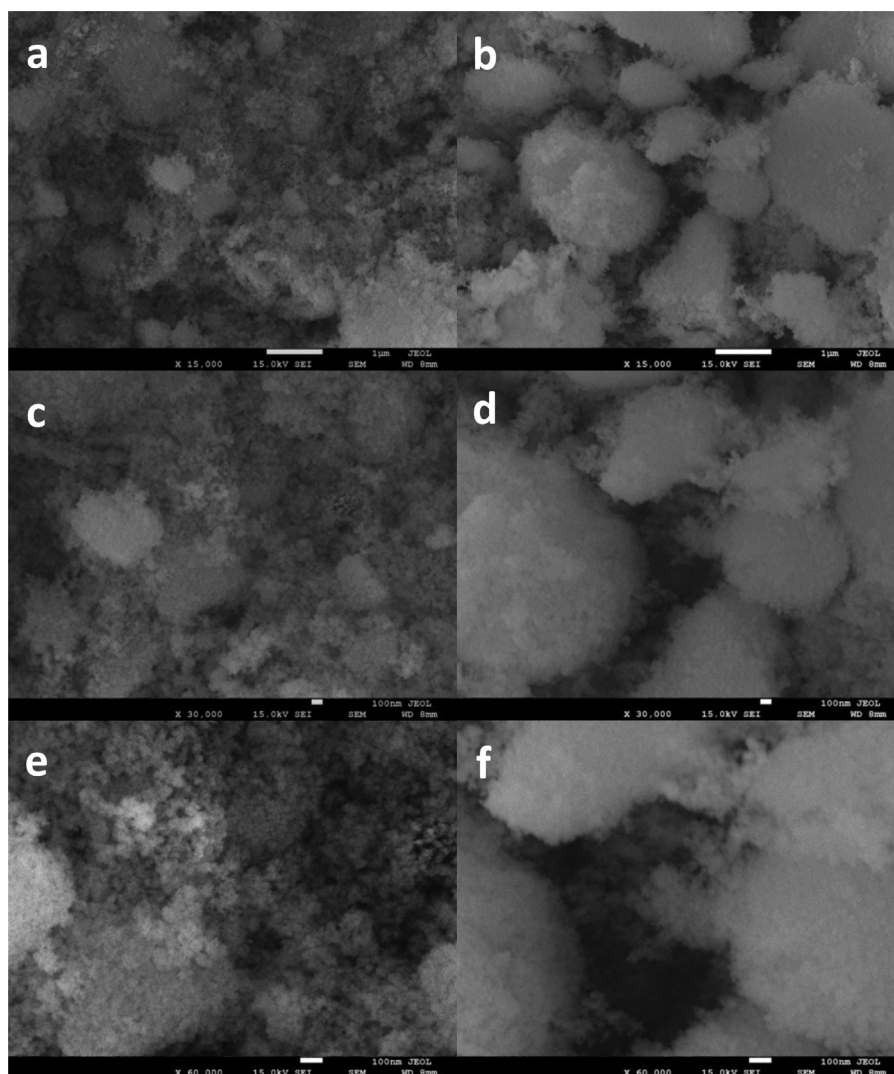


Fig. 6. The FESEM images of unexposed (a,c,e) and exposed (b,d,f) CeO₂ at 15,000 \times , 30,000 \times and 60,000 \times .

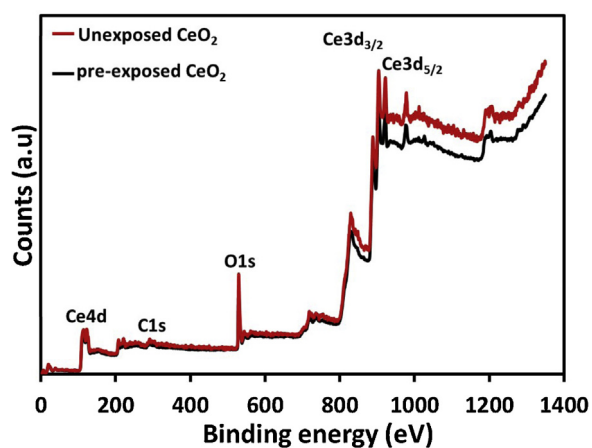


Fig. 7. The comparison of the XPS survey scans of unexposed and exposed CeO₂.

the electrical resistance of the pure and exposed CeO₂ electrodes was much lower under illumination. The absence of the semicircular part in the higher frequency region of EIS spectrum depicted the high electron transport efficiency of the pure and sunlight exposed CeO₂ electrodes. The low impedance part at the higher frequency was exploded and presented in the inset of Fig. 10a. The higher

electrical response of the exposed CeO₂ under illumination may be attributed to the transfer of excited electrons to the photon induced defects.

The two step chronopotentiometric measurements of pristine and sunlight exposed CeO₂ were performed both in the dark and under illumination. The galvanostatic charge–discharge profile of

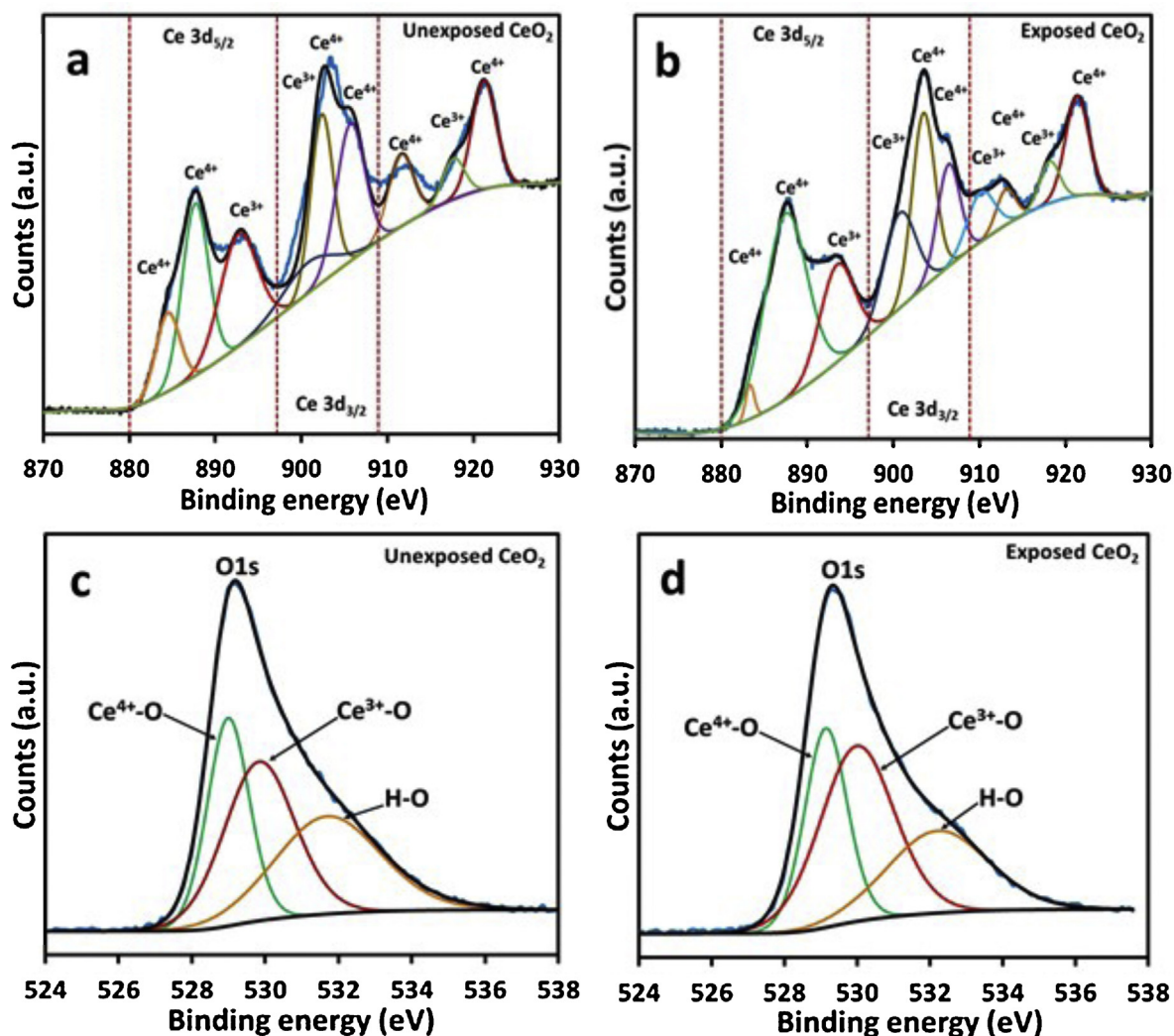


Fig. 8. The comparison of fitted Ce 3d and O 1s levels of unexposed (a and c) and exposed (b and d) CeO₂. (For interpretation of the references to color mention in the text, the reader is referred to the web version of this article.)

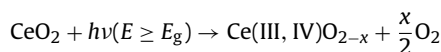
unexposed and exposed CeO₂ is shown in Fig. 10b, where the unsymmetrical curves for both pure and exposed CeO₂ indicated the pseudo-capacitive characteristics of the material as marked from the CV patterns [54]. As compared to the pristine the slow discharge behavior of sunlight exposed CeO₂ suggest the prolonged lifetime of the excited states and improved electron retention capability of exposed CeO₂ under illumination. A similar findings were observed in the PL analysis of the unexposed and exposed samples. The specific capacitance of unexposed and exposed CeO₂ discharge curves was evaluated by using the relation mentioned below.

$$C_s = \frac{I \times \Delta t}{m \times \Delta V}$$

The evaluated C_s of pure and exposed CeO₂ under illumination were 0.438 F g⁻¹ and 0.507 F g⁻¹, respectively, highlighted that the specific capacitance of CeO₂ is enhanced after exposure to sunlight.

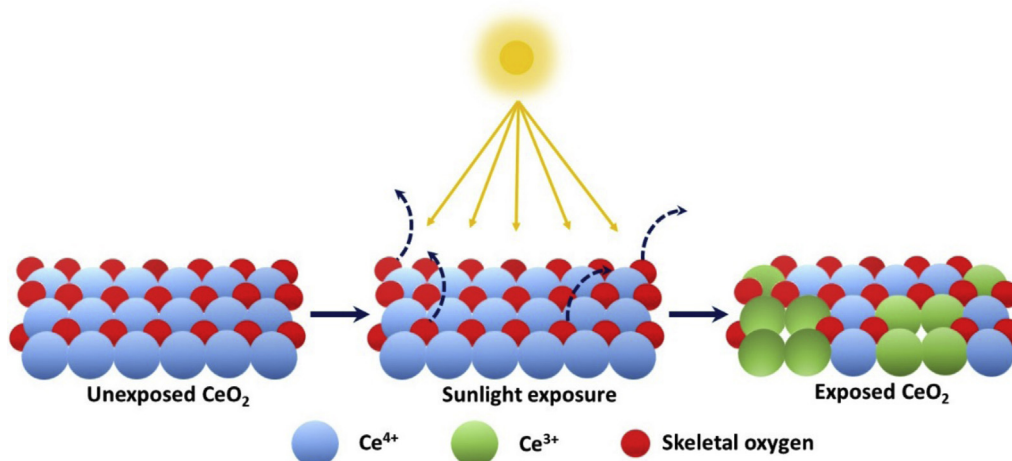
Based on all the evidences discussed above, it was presumed that the interaction of UV photons of sunlight with CeO₂ resulted in the departure of labile skeletal oxygen thus forming CeO_{2-x} based defects. The departure of oxygen from Ce⁴⁺-8O octahedra results in the variations of the oxidation state of corresponding Ce atom for

stable configuration. The same may be represented by the relations presented below.



The assumption of the loss of oxygen with the possible formation of surface CeO_{2-x}, under illumination, was further investigated by thermo-gravimetric analysis (TGA). The comparison of the TG patterns (weight loss (%)) versus temperature) of unexposed and exposed CeO₂ in the temperature range of 50–900 °C is presented in Fig. 11. To observe the possible effect of oxygen environment with increasing temperature, the patterns were recorded in air rather than inert atmosphere. The careful analysis of the results revealed that oxygen interact with both the materials in the temperature range of 350–550 °C however, the magnitude of the oxygen insertion for sunlight exposed CeO₂ was higher than that of unexposed sample. The same is marked by dotted lines in the Fig. 11. This evidence authenticated the formation of CeO_{2-x} surface defects with the loss of oxygen by photon interaction. Pictorially, the formation of CeO_{2-x} states can be represented as follows in Scheme I.

The lower activity of CeO₂ for the degradation/mineralization of phenol and its derivatives, in the initial 60–90 min of sunlight exposure, was attributed to the fact that during this period the majority of the incident photons are consumed in the induction of surface



Scheme 1. The plausible mechanisms for the formation of CeO_{2-x} states in sunlight exposure.

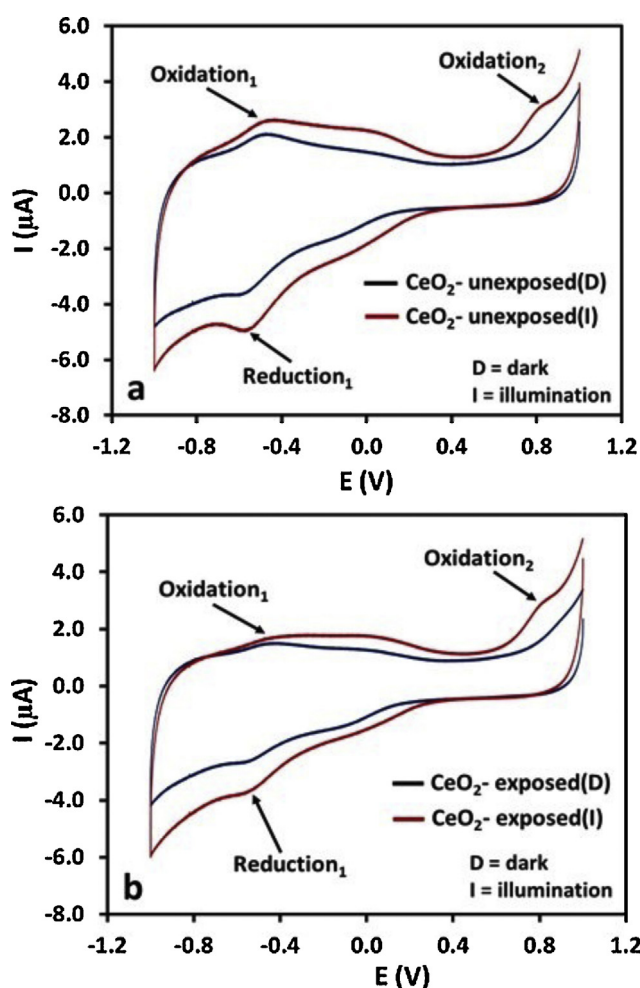


Fig. 9. The comparison of the cyclic voltammograms of (a) unexposed (b) sunlight exposed CeO_2 in the dark and under illumination.

defects. The degradation/mineralization of the substrates is radically increased as the surface density of surface defects reaches to an appreciable extent that concluded the prolific role of photon induced CeO_{2-x} phases (defects) in the enhanced formation of ROS. Moreover, it might be presumed that the departure of skeletal oxygen significantly disturbs the stoichiometry of Ce^{4+} and Ce^{3+} entities at the surface. The prevalence of low energy

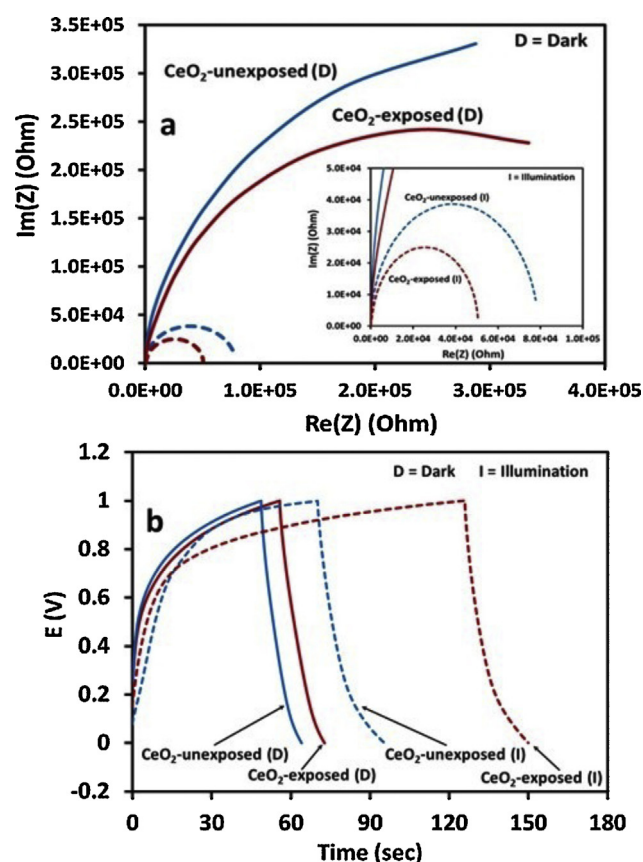


Fig. 10. The comparison of the (a) EIS response (b) The charge–discharge curve of unexposed and exposed CeO_2 in dark and under illumination. The inset of (a) shows the exploded view of the EI spectra of both under illumination.

transitions are noticeably evidenced by the solid-state absorption spectra (Fig. 3a), whereas the decreased emission intensity of the exposed compared to un-exposed CeO_2 samples in the PL analysis (Fig. 3b) undoubtedly validated the trapping of the excited electrons by the Ce^{3+} states. Based on the above evidences, it was inferred that the induces Ce^{3+} states not only serve as photo-excited electron trap centers but also share the valence band to facilitate the direct transition from O ($2p$) to Ce^{3+} ($4f^1$) thus generating low energy transitions. Therefore, the sunlight induced Ce^{3+} states add an extra low energy conduction band composed of Ce^{3+} ($4f^1$) states besides that of the already existing Ce^{4+} ($4f^0$) however, the

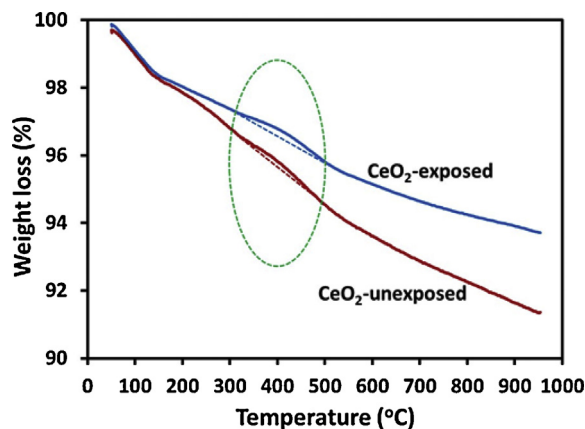
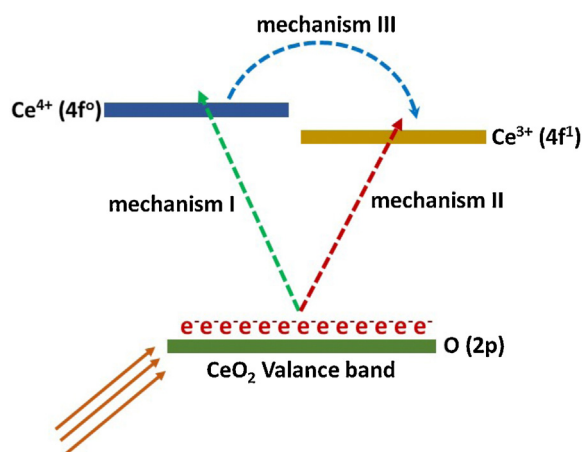


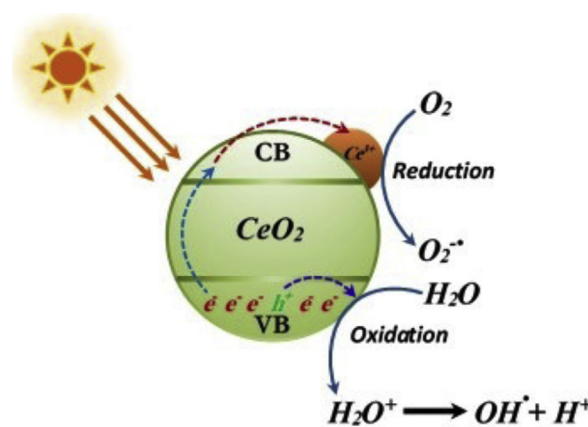
Fig. 11. The comparison of the TG patterns (weight loss) of unexposed and sunlight exposed CeO₂ in the temperature range of 50–950 °C in air.



Scheme II. The plausible mechanisms of inhibition of charge carrier recombination process by the CeO_{2-x} surface defects.

effectiveness of the additional conduction band in enhancing the photocatalytic degradation process or generation of ROS is based on the surface population of Ce³⁺ (4f¹) in the form of CeO_{2-x} defects (Schemes I and II). Another plausible mode of prolonging the lifetime of the excitons is the mutual transfer of the excited electrons from Ce⁴⁺ (4f⁰) to closely spaced Ce³⁺ (4f¹) states to form Ce⁴⁺ (4f¹) (Scheme III). Based on the stability consideration the prolonged quiescent of the electrons in this state is highly unlikely therefore, transferred to reductants instantaneously for the generation of ROS in the system. Additionally, the positive valence band and negative conduction band potential than that of Ce⁴⁺/Ce³⁺ couple (1.3–1.8 V) suppresses the carrier charge recombination by the mutual transfer of electrons between Ce⁴⁺ and Ce³⁺ states hence accelerating the degradation and mineralization process significantly [55]. The possible mechanisms of the inhibition of the recombination process and the formation of ROS (O₂^{•-} or HO[•]) can be pictorially explained in Schemes II and III.

Fig. 12 shows the effect of the UV photon induced surface phases on the photocatalytic activity for the degradation of 2-NP where it can be observed that the presence of surface phases significantly enhanced the photocatalytic activity in the visible region of the sunlight compared to unexposed CeO₂. Compared to ~70% for unexposed CeO₂ in 180 min of exposure of visible region of sunlight, the exposed CeO₂ (CeO_{2-x}@CeO₂) degraded ~92% of 2-NP in the same period. Similar to the degradation of 2-NP over unexposed CeO₂ in the visible region, the rate of degradation over exposed CeO₂ (inset of Fig. 12), followed the Langmuir–Hinshelwood kinetic



Scheme III. The plausible mechanisms for the generation of ROS for the CeO₂ with surface CeO_{2-x} defects.

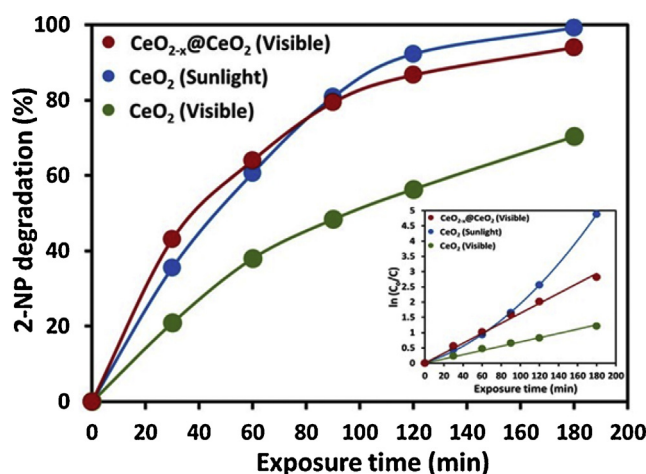


Fig. 12. The comparison of the 2-NP (50 ppm) degradation of unexposed CeO₂ in complete spectrum sunlight with unexposed and exposed CeO₂ (3 h) in the visible portion (420–800 nm) of sunlight. The inset shows the graphical evaluation of the rate of degradation for the same materials.

model. However, the comparison of the degradation patterns revealed the importance of UV region of sunlight in enhancing the photocatalytic activity cannot be ignored.

As mentioned earlier a significant variation in the rate of degradation of phenol, 2-CP, 2-BP and 2-NP was noticed in the sunlight exposure over CeO₂. This observation led to the perception regarding the probable involvement of charged ROS i.e. superoxide anions (O₂^{•-}), in the degradation process. Phenol being the least degraded possesses a negatively charged surface as result of its weak dissociation and formation of enolate anion in aqueous medium. The delocalization of the charge on oxygen on the aromatic system impart excessive negative charge to the aromatic ring that repels the incoming singly negatively charged superoxide radicals thus low degradation is observed. The presence of hydroxy phenols (pyrocatechol, resorcinol or hydroquinone) as intermediates in the degradation of phenol depicted that the observed initial degradation of phenol is carried out by HO[•] rather than O₂^{•-}. The extent of the negative charge is reduced with the induction of hydroxyl groups in the aromatic system that increases the possibility of superoxide interaction. In the other substrates i.e. 2-CP, 2-BP and 2-NP, the substituents attached to the aromatic system distort the electronic cloud by inductive effect, thus generating the active sites bearing partial positive charge for O₂^{•-} attack. Based on the identification of aliphatic oxygenates as intermediates, it can be speculated that the substituent bearing carbon atom (2- position in

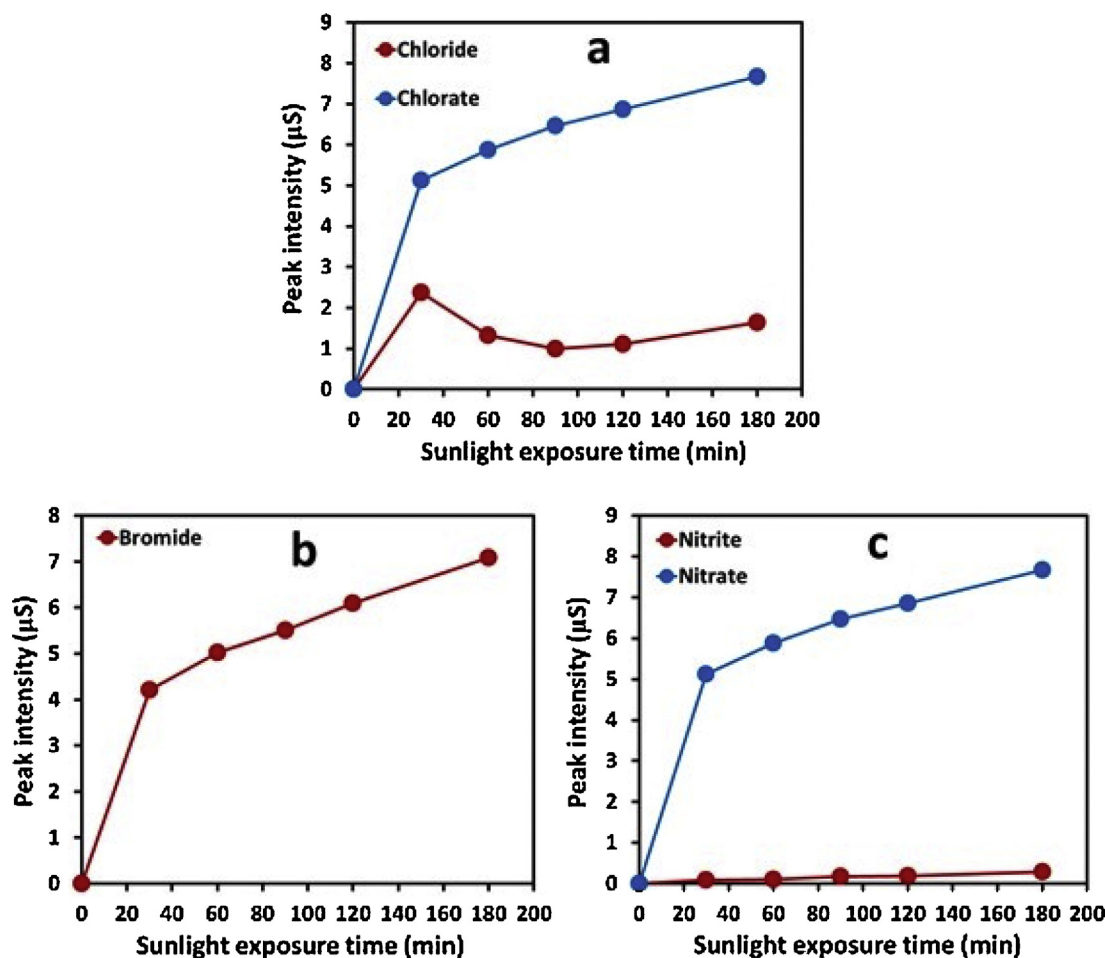
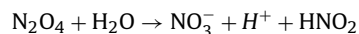
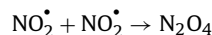
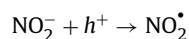


Fig. 13. The time scale profiles for the release of ion in the degradation of (a) 2-CP (b) 2-BP and (c) 2-NP in the exposure of complete spectrum sunlight.

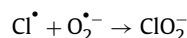
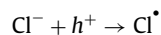
this case) is interacted by $O_2^{\bullet-}$ displacing the attached substituent with the self-insertion and ring opening. The rate of degradation of a particular substrate is dependent on its ability to distort electronic cloud for the generation of sites. Among the substrates under study, 2-NP, proved to be the most efficient in facilitating is self-degradation. The difference in the degradation of 2-CP and 2-BP may be attributed to the size of Cl and Br groups. It was noticed that besides photocatalytic process, the degradation of 2-BP is also incurred by photolysis in the exposure to complete spectrum sunlight, however, a low mineralization was observed in the photolysis. Additionally, the magnitude of photolysis was significantly lower in the visible region of sunlight.

The assumption that the substituents are replaced by the superoxide anions ($O_2^{\bullet-}$), was further verified by measuring the ions released during the degradation of 2-CP, 2-BP and 2-NP by ion chromatography. The time-scale IC profiles for the degradation of 2-CP, 2-BP and 2-NP in the complete spectrum sunlight exposure are presented in Figs. S4–6 (Supporting information). A minor concentration of Cl^- and NO_2^- ions was noticed in the solution while ClO_2^- and NO_3^- were identified as major components in the degradation of 2-CP and 2-NP. This observation led to the inference that Cl^- and NO_2^- are instantaneously transformed to ClO_2^- and NO_3^- ions, respectively, while the presence of Br^- ions in the solution depicted no further interaction either with ROS present in the solution or photogenerated holes (h^+). The comparison of the time scale release of anions during the degradation of 2-CP, 2-BP and 2-NP is presented in Fig. 13a–c, where an instantaneous transformation of NO_2^- to NO_3^- and Cl^- to ClO_2^- is evident while Br^-

ions do not undergo further interaction. The profiles also depicted the varying degree of secondary interactions between the primary displaced ions and ROS. Being negatively charged, the direct interaction between the released primary ions is energetically forbidden process, therefore, as explained below, it is proposed that the released anions initially interact with the photogenerated holes and finally with the $O_2^{\bullet-}$.



Similarly,



The interaction of the primary released ions with the photon generated excited entities at varying degree suggest that the nature, the oxidation potential of the ions involved and the potential of the valence band edge are the key controlling factors in this regard.

4. Conclusions

The study revealed the importance of the minor UV portion of the sunlight (<5%) in inducing the surface defects at the surface of CeO_2 . The CeO_{2-x} surface defects serve as the trap and transfer

centers and promote the transfer of excited electrons to the reductants for the enhanced generation of ROS. The change in surface stoichiometry and the formation of the defects may not be correlated with the instability of CeO₂ under illumination as these changes are stable at room temperature, whereas reversible at elevated temperatures. The formation of defects does not affect the bulk properties of CeO₂, however improves the desired optical properties such as better absorption photocatalytic properties and prolonged lifetime of the excited states for better photocatalytic performance. Based on various experimental observations such as rapid mineralization and the released ions in the solution, superoxide anion radicals were identified as major contributors in degradation/mineralization process. The degradation of phenol derivatives is influenced by the nature of the substituents attached to the aromatic system. The released anions are further interacted by either ROS or the photogenerated holes leading to additional ions.

Acknowledgements

Authors are greatly indebted to the Center of Excellence in Environmental Studies (CEES), King Abdulaziz University and Ministry of Higher Education (MoHE), Kingdom of Saudi Arabia, for their supports.

Appendix A. Supplementary data

Supplementary data associated with this article can be found, in the online version, at <http://dx.doi.org/10.1016/j.apcatb.2015.06.050>

References

- [1] H. Suty, C. De Traversay, M. Cost, *Water Sci. Technol.* 49 (2004) 227–233.
- [2] J. Schneider, M. Matsuoka, M. Takeuchi, J. Zhang, Y. Horiuchi, M. Anpo, D.W. Bahnemann, *Chem. Rev.* 114 (2014) 9919–9986.
- [3] A. Mills, R.H. Davies, D. Worsley, *Chem. Soc. Rev.* 22 (1993) 417–425.
- [4] M.R. Hoffmann, S. Martin, W. Choi, D.W. Bahnemann, *Chem. Rev.* 95 (1995) 69–96.
- [5] M.T. Qamar, M. Aslam, I.M.I. Ismail, N. Salah, A. Hameed, *ACS Appl. Mater. Interfaces* 7 (2015) 8757–8769.
- [6] U.I. Gaya, A.H. Abdullah, *J. Photochem. Photobiol. C: Photochem. Rev.* 9 (2008) 1–12.
- [7] S.G. Kumar, K.S.R. Koteswara Rao, *RSC Adv.* 5 (2015) 3306–3351.
- [8] S. Rehman, R. Ullah, A.M. Butt, N.D. Gohar, *J. Hazard. Mater.* 170 (2009) 560–569.
- [9] A. Fujishima, T.N. Rao, D.A. Tryk, *J. Photochem. Photobiol. C: Photochem. Rev.* 1 (2000) 1–21.
- [10] M. Aslam, I.M.I. Ismail, S. Chandrasekaran, H.A. Qari, A. Hameed, *Water Air Soil Pollut.* 226 (2015) 70.
- [11] I.M.I. Ismail, M. Aslam, T. Almelbi, S. Chandrasekaran, A. Hameed, *RSC Adv.* 4 (2014) 16043–16046.
- [12] A. Hameed, T. Montini, V. Gombac, P. Fornasiero, *J. Am. Chem. Soc.* 130 (2008) 9658–9659.
- [13] A. Hameed, M. Aslam, I.M.I. Ismail, N. Salah, P. Fornasiero, *Appl. Catal. B: Environ.* 163 (2015) 444–451.
- [14] M. Aslam, I.M.I. Ismail, S. Chandrasekaran, A. Hameed, *J. Hazard. Mater.* 276 (2014) 120–128.
- [15] M. Aslam, I.M.I. Ismail, N. Salah, S. Chandrasekaran, M.T. Qamar, A. Hameed, *J. Hazard. Mater.* 286 (2015) 127–135.
- [16] M.D.H. Alonso, A.B. Hungria, A.M. Arias, M.F. Garcia, J. Coronado, J.C. Conesa, *J. Soria, Appl. Catal. B* 50 (2004) 167–175.
- [17] M.A. Lazar, S. Varghese, S.S. Nair, *Catalysts* 2 (2012) 572–601.
- [18] Y.Q. Zhai, S.Y. Zhang, H. Pang, *Mater. Lett.* 61 (2007) 1863–1866.
- [19] P. Borker, A.V. Salker, *Mater. Chem. Phys.* 103 (2007) 366–370.
- [20] M.J. Muñoz-Batista, A. Kubacka, M.N. Gómez-Cerezo, D. Tudela, M. Fernández-García, *Appl. Catal. B: Environ.* 140–141 (2013) 626–635.
- [21] C. Karunakaran, R. Dhanalakshmi, *Sol. Energy Mater. Sol. Cells* 92 (2008) 1315–1321.
- [22] Y. Yavuz, A.S. Kopal, *J. Hazard. Mater.* 136 (2006) 296–302.
- [23] A. Bodalao, J.L. Gómez, M. Gómez, G. León, A.M. Hidalgo, M.A. Ruiza, *Desalination* 223 (2008) 323–329.
- [24] G. Busca, S. Berardinelli, C. Resini, L. Arrighi, *J. Hazard. Mater.* 160 (2008) 265–288.
- [25] V.M. Egorov, S.V. Smirnova, I.V. Pletnev, *Sep. Purif. Technol.* 63 (2008) 710–715.
- [26] F. Gea, L. Zhu, J. Wang, *Desalination* 225 (2008) 156–166.
- [27] A.T. Mohd Din, B.H. Hameed, A.L. Ahmad, *J. Hazard. Mater.* 161 (2009) 1522–1529.
- [28] A. Rubalcaba, M.E. Suárez-Ojedaa, J. Carrerab, J. Fonta, F. Stübera, C. Bengoaa, A. Fortunc, A. Fabregata, *Catal. Today* 124 (2007) 191–197.
- [29] M.E. Suarez, A. Fabregat, F. Stüber, A. Fortunc, J. Carrera, J. Font, *Chem. Eng. J.* 132 (2007) 105–115.
- [30] M. Wagner, J.A. Nicell, *Water Res.* 36 (2002) 4041–4052.
- [31] U.S. Environmental Protection Agency, *Ambient Water Quality Criteria for Nitrophenols*, U.S. Environmental Protection Agency, Washington, DC, 1980.
- [32] S.S. Adav, M.Y. Chen, D.J. Lee, N.Q. Ren, *Chemosphere* 67 (2007) 1566–1572.
- [33] N. Calace, E. Nardi, B.M. Petronio, M. Pietroletti, *Environ. Pollut.* 118 (2002) 315–319.
- [34] J. Yang, S. Cui, J. Qiao, H. Lian, *J. Mol. Catal. A: Chem.* 395 (2014) 42–51.
- [35] O.A. O'Connor, L.Y. Young, *Environ. Toxicol. Chem.* 8 (1989) 853–861.
- [36] M. Aslam, I.M.I. Ismail, T. Almelbi, S. Chandrasekaran, A. Hameed, *Chemosphere* 117C (2014) 115–123.
- [37] M. Czaplicka, *Sci. Total Environ.* 322 (2004) 21–39.
- [38] M. Aslam, I.M.I. Ismail, S. Chandrasekaran, T. Almelbi, A. Hameed, *RSC Adv.* 4 (2014) 49347–49359.
- [39] M. Aslam, M.T. Soomro, I.M.I. Ismail, N. Salah, M.W. Ashraf, H.A. Qari, A. Hameed, *Arabian J. Chem.* (2015) <http://dx.doi.org/10.1016/j.arabjc.2015.05.001>
- [40] R.M. Bashami, A. Hameed, M. Aslam, I.M.I. Ismail, M.T. Soomro, *Anal. Methods* 7 (2015) 1794–1801.
- [41] P. Pichat, *Photocatalysis and Water Purification: From Fundamentals to Recent Applications*, 1st ed., Wiley-VCH Verlag, GmbH Germany, 2013.
- [42] B. Choudhury, P. Chetri, A. Choudhury, *RSC Adv.* 4 (2014) 4663–4671.
- [43] J. Strunk, W.C. Vining, A.T. Bell, *J. Phys. Chem. C* 115 (2011) 4114–4126.
- [44] M. Kong, Y.Z. Li, X. Chen, T. Tian, P. Fang, F. Zhang, X. Zhao, *J. Am. Chem. Soc.* 133 (2011) 16414–16417.
- [45] A. Hameed, M. Aslam, I.M.I. Ismail, S. Chandrasekaran, M.W. Kadi, M.A. Gondal, *Appl. Catal. B: Environ.* 160–161 (2014) 227–239.
- [46] A. Trovarelli, *Catalysis by Ceria and Related Materials*, Imperial College Press, London, 2002.
- [47] W.Q. Han, L. Wu, Y. Zhu, *J. Am. Chem. Soc.* 127 (2005) 12814–12815.
- [48] L. Ma, D. Wang, J. Li, B. Bai, L. Fu, Y. Li, *Appl. Catal. B: Environ.* 148–149 (2014) 36–43.
- [49] E. Abi-Aad, R. Bechara, J. Grimbolt, A. Aboukais, *Chem. Mater.* 5 (1993) 793–797.
- [50] C. Anandan, P. Bera, *Appl. Surf. Sci.* 283 (2013) 297–303.
- [51] (a) C.O. Avellaneda, M.A.C. Berton, L.O.S. Bulhões, *Sol. Energy Mater. Sol. Cells* 92 (2008) 240–244;
(b) Y. Fu, Z.D. Wei, M.B. Ji, L. Li, P.K. Shen, J. Zhang, *Nanoscale Res. Lett.* 3 (2008) 431–434;
(c) F. Kiani, A.A. Rostami, F. Gharib, S. Sharifi, A. Bahadory, *J. Chem. Eng. Data* 56 (2011) 2830–2835.
- [52] F. Kiani, M. Sharifirad, N. Yazdizadeh, F. Koohyar, *Iran. J. Energy Environ.* 2 (2011) 215–220.
- [53] (a) R. Velmurugan, B. Sreedhar, M. Swaminathan, *Chem. Cent. J.* 5 (2011) 46;
(b) J. Zheng, H. Yu, X. Li, S. Zhang, *Appl. Surf. Sci.* 254 (2008) 1630–1635.
- [54] (a) B. Yin, S. Zhang, Y. Jiao, Y. Liu, F. Qu, X. Wu, *Cryst. Eng. Commun.* 16 (2014) 9999–10005;
(b) P. Yang, X. Xiao, Y. Li, Y. Ding, P. Qiang, X. Tan, W. Mai, Z. Lin, W. Wu, T. Li, H. Jin, P. Liu, J. Zhou, C.P. Wong, Z.L. Wang, *ACS Nano* 7 (2013) 2617–2626.
- [55] A. Paulenova, S.E. Creager, J.D. Navratil, Y. Wei, *J. Power Sources* 109 (2002) 431–438.